

### **MALAYSIAN JOURNAL OF ANALYTICAL SCIENCES**

ANALIS

Journal homepage: https://mjas.analis.com.my/

# Research Article

Adsorptive removal of methylene blue using magnetic graphitic carbon nitride  $(Fe_3O_4/g-C_3N_4)$  composite: insights into isotherms, kinetics, and thermodynamic properties

Nurul Izza Taib<sup>1</sup>, Rozaina Saleh<sup>1,2\*</sup>, Aunie Aqelah Fisol<sup>1</sup>, Isma Iwana Ismail<sup>1</sup>, and Nur Najieha Ismail<sup>1</sup>

<sup>1</sup>Faculty of Applied Sciences, Universiti Teknologi MARA, Perak Branch, Tapah Campus, 35400 Tapah Road, Perak, Malaysia

<sup>2</sup>Faculty of Applied Sciences, Universiti Teknologi MARA, 40450 Shah Alam, Selangor Darul Ehsan, Malaysia

\*Corresponding author: rozaina103@uitm.edu.my

Received: 19 September 2024; Revised: 9 December 2024; Accepted: 14 December 2024; Published: 8 April 2025

#### Abstract

In the present study, we have successfully synthesized iron oxide-coated graphitic carbon nitride (g-C<sub>3</sub>N<sub>4</sub>/Fe<sub>3</sub>O<sub>4</sub>) through chemical co-precipitation and utilized it as an adsorbent for removing methylene blue (MB) from an aqueous solution. These findings demonstrate the effectiveness of g-C<sub>3</sub>N<sub>4</sub>/Fe<sub>3</sub>O<sub>4</sub> as an adsorbent for removing cationic dyes from aqueous solutions. The as-prepared composites underwent a thorough characterization using X-ray powder diffraction (XRD), Field Emission Scanning Electron Microscopy (FESEM), Fourier Transform Infrared (FTIR), Zeta Potential and Vibrating Sample Magnetism (VSM). XRD and FTIR have confirmed the formation of composites of g-C<sub>3</sub>N<sub>4</sub>/Fe<sub>3</sub>O<sub>4</sub>. FESEM verifies the nano-scale nature of the composite. From VSM, the composite has high saturation magnetization, which implies that the adsorbent can be separated from the treated solution by employing an external magnet. The removal percentage of MB was evaluated under various conditions, including pH (2.0 -8.0), contact time (10 - 360 min), initial concentration (10 - 300 mg/L), and temperature (298 K - 328 K), using batch-adsorption techniques. This study found that the optimal pH for adsorption was 5.0, with the highest adsorption capacity observed at the concentration of 10 mg/L, achieving an 81.11% removal efficiency. Equilibrium adsorption reached 45.58% within 30 minutes. The Langmuir isotherm which can explain the adsorption isotherms, indicate maximum adsorption capacity of 40.2 mg/g. Kinetic studies indicated that the adsorption process conformed to a pseudo-second-order model, suggesting a chemical sorption involvement. Thermodynamic analysis revealed a positive Gibbs free energy value, indicating a non-spontaneous reaction, and a positive enthalpy value, suggesting an endothermic process.

**Keywords:** iron oxide; graphitic carbon nitride; adsorption; thermodynamics; isotherms

# Introduction

The growing concern regarding organic water contamination, mainly due to the presence of dyes, has become a central and urgent topic in environmental and public health discussions. The harmful impacts of these pollutants to the ecosystems and human health highlight the immediate need to address these issues promptly. The textile industry, a major contributor to the global water pollution, requires immediate attention and the implementation of effective mitigation strategies [1-3]. The activities of this industry have led to a rise in the number of polluted rivers over time, emphasizing the need for effective mitigation strategies [2, 4].

Methylene blue (MB), a prominent cationic dye with molecular formula  $C_{16}H_{18}CIN_3S$ [5] poses environmental challenges due to its intricate molecular structure, which hinders breakdown processes, making it challenging to be removed through conventional wastewater treatment methods [6]. It is typically used for biological staining techniques, calico printing, and the dyeing of wool, cotton, leather, silk, and textile. It produces a visible hue at concentrations as low as 1 mg/L, and is categorized as a hazardous colorant [7, 8]. Despite its versatility in colouring, MB is considered a hazardous colorant with adverse ecological and aesthetic implications when discharged into water bodies [8, 9]. Methylene blue in wastewater obstructs

the penetration of sunlight, diminishing the capacity of aquatic plants from receiving light, thus reducing oxygen levels in water bodies and inhibiting the photosynthetic process of aquatic flora. Additionally, the presence of MB poses health risks to humans, leading to symptoms like nausea, eye irritation, and digestive discomfort [9, 10]. Given its hazardous nature and harmful impacts on human health and the environment, efficient and affordable processes to remove MB from wastewater are urgently needed.

Various conventional techniques, including ion exchange [11], membrane filtration [12], reverse osmosis [13], and electrochemical treatment [14, 15], with varying degrees of success, have been done to remove pollutants from wastewater. The most efficient and practical method for removing pollutants is adsorption due to its affordability and suitability for large-scale applications [16-18]. One major advantage is the low energy consumption associated with the adsorption processes, making it a cost-effective solution for pollutant removal. Additionally, adsorption methods are known for their ease of operation, environmental friendliness, and the absence of secondary pollution, making them a sustainable choice for wastewater treatment [19].

Graphitic carbon nitride (g-C<sub>3</sub>N<sub>4</sub>) is a twodimensional conjugated polymer that has attracted a significant attention due to its unique properties and potential applications. It can be synthesized through the polycondensation of organic precursors such as melamine, dicyandiamide, urea, and cyanamide, or even by the mixture of urea and melamine [20, 21]. It exhibits intrinsic semiconducting properties with a geometric configuration featuring a superimposed heterocyclic sp<sup>2</sup> carbon and nitrogen framework connected via tri-s-triazine-based patterns, a nonplanar layer chain structure, and alternating buckling [22, 23]. It is known for its low-cost synthesis, high stability, and unique electronic properties. g-C<sub>3</sub>N<sub>4</sub> is a metal-free catalyst with a high quantum yield, nontoxicity, and electron-rich properties [24]. It is highly stable in an ambient atmosphere and possesses rich surface properties that are attractive for catalysis due to the presence of basic surface sites [25, 26]. Additionally, g-C<sub>3</sub>N<sub>4</sub> is resistant to acid, alkalis, and high temperatures due to the strong covalent bonds between carbon and nitrogen atoms [27]. Moreover, g-C<sub>3</sub>N<sub>4</sub> exhibits an adjustable band structure, is readily available in large quantities, possesses low toxicity, and demonstrates robust stability, making it an environmentally friendly option with attractive features [28].

The adsorption capacity of g-C<sub>3</sub>N<sub>4</sub> is limited by its inert properties, restricting its ability to adsorb

certain molecules. The inert nature of g-C<sub>3</sub>N<sub>4</sub> may lead to a reduced adsorption of molecules such as water or oxygen, thereby impacting its catalytic performance [29]. This drawback can hinder its effectiveness in adsorption-based applications, particularly when targeting specific molecules for removal from a solution. Furthermore, the structure of g-C<sub>3</sub>N<sub>4</sub> may not be optimized for an efficient adsorption of certain compounds. Modifications or enhancements are necessary to enhance its adsorption capabilities for a variety of adsorbates, such as improving its porous structure to increase surface area and reactivity [30].

The synthesizing of Fe<sub>3</sub>O<sub>4</sub> nanoparticles is very easy, cheap, scalable, and easy to functionalize with other materials [31-33]. Fe<sub>3</sub>O<sub>4</sub> nanoparticles have become one of the popular choices to be integrated with g-C<sub>3</sub>N<sub>4</sub> due to their high saturation magnetization. This property allows them to exhibit magnetic properties with the presence of an external magnetic [21, 34]. The integration of g-C<sub>3</sub>N<sub>4</sub> with magnetic materials, such as Fe<sub>3</sub>O<sub>4</sub>, enhances the adsorption capacity [35] and makes it easier to separate the adsorbent from the treated water using an external magnetic field [21]. The utilization of Fe<sub>3</sub>O<sub>4</sub> nanoparticles not only facilitates easy separation but also minimizes secondary contamination and reduces Composite materials, such as magnetic graphitic carbon nitride (Fe<sub>3</sub>O<sub>4</sub>/g-C<sub>3</sub>N<sub>4</sub>), have emerged as a viable approach for the removal of pollutants, providing sustainable and efficient solutions for wastewater treatment [35-37].

The composite material of g-C<sub>3</sub>N<sub>4</sub> with magnetite demonstrated an impressive adsorption capacity of 169 mg/g [37]. Due to its magnetic properties, the incorporation of magnetite into the g-C<sub>3</sub>N<sub>4</sub> matrix significantly enhances the adsorption capacity and simplifies the separation process. Georgiou et al. [36] mentioned the evolution of iron phases on the aminerich carbon nitride surface enhances the adsorption capacity of the g-C<sub>3</sub>N<sub>4</sub>, making it a promising candidate for arsenic removal applications. The magnetic g-C<sub>3</sub>N<sub>4</sub> composite, due to its positive charge, has the ability to adsorb arsenate (III) anions, which are negatively charged solutes.

While there has been significant progress in exploring various adsorbents for dye removal from wastewater, the application of composite materials of g-C<sub>3</sub>N<sub>4</sub>/Fe<sub>3</sub>O<sub>4</sub> as effective adsorbent remains relatively underexplored. Despite the promising photocatalytic and magnetic properties of g-C<sub>3</sub>N<sub>4</sub> and Fe<sub>3</sub>O<sub>4</sub> respectively, studies focusing on the potential of composite for dye adsorption are still limited. This gap presents an opportunity to investigate the

efficiency of g-C<sub>3</sub>N<sub>4</sub>/Fe<sub>3</sub>O<sub>4</sub> composites as effective adsorbents, thereby contributing to the growing body of research in environmental remediation. This study aims to address this gap by investigating the adsorption efficiency of g-C<sub>3</sub>N<sub>4</sub>/Fe<sub>3</sub>O<sub>4</sub> in dye removal, offering a complementary approach to wastewater treatment. Thus, g-C<sub>3</sub>N<sub>4</sub>/Fe<sub>3</sub>O<sub>4</sub> composite was utilized as the adsorbent for the removal of MB, a very hazardous aromatic organic contaminant, from an aqueous solution. The batch adsorption tests were conducted to determine the maximum adsorption capacity of MB onto the surface of g-C<sub>3</sub>N<sub>4</sub>/Fe<sub>3</sub>O<sub>4</sub>. A plausible mechanism for the interaction of MB on the surface of g-C<sub>3</sub>N<sub>4</sub>/Fe<sub>3</sub>O<sub>4</sub> surface was postulated.

### Materials and Methods Materials

Urea A.R. (R&M Chemicals), Iron (II) Chloride Tetrahydrate C.P. (R&M Chemicals), Iron (III) Hexahydrate A.R. (R&M Chemicals), Ethanol (70%, Systerm), Ammonium Hydroxide (30%, R&M Chemicals), and Methylene Blue (R&M Chemicals) were used as received without any further treatment or purification.

### Preparation of g-C<sub>3</sub>N<sub>4</sub>/Fe<sub>3</sub>O<sub>4</sub> composite

The g-C<sub>3</sub>N<sub>4</sub> was prepared using the thermal polymerization method. A crucible containing 10.0 g of urea was heated in a furnace to 550°C at a 2°C/min rate for 3 hours. After cooling at ambient temperature, the yellow product was ground into a fine powder and stored for further use. Next, the g-C<sub>3</sub>N<sub>4</sub>/Fe<sub>3</sub>O<sub>4</sub> composite was synthesized using a mass ratio of 2:1 of g-C<sub>3</sub>N<sub>4</sub> to Fe<sub>3</sub>O<sub>4</sub>. In brief, 0.8 g-C<sub>3</sub>N<sub>4</sub> was dispersed in a mixture of 60 ml of ethanol and 120 ml of water in a round bottom flask. The yellow suspension was sonicated for 30 minutes to achieve a homogeneous solution. Subsequently, 0.9340 g of FeCl<sub>3</sub>.6H<sub>2</sub>O and 0.3436 g of FeCl<sub>2</sub>.4H<sub>2</sub>O were dissolved with 100 ml of distilled water in a beaker.

Then, the solution was added to a round bottom flask. Then, the suspension was stirred for 30 minutes at 80°C. Following this, 10 ml of 30% NH<sub>3</sub> was introduced drop by drop to the mixture under a vigorous stirring. After 60 minutes of stirring, a dark brown suspension of g-C<sub>3</sub>N<sub>4</sub>/Fe<sub>3</sub>O<sub>4</sub> composite was obtained. After cooling at room temperature, the mixture was washed twice with water and ethanol before being magnetically separated. The dark brown precipitate was obtained and dried in an oven for 12 hours at 70°C.

# Characterization of g-C<sub>3</sub>N<sub>4</sub>/Fe<sub>3</sub>O<sub>4</sub> composite

The functional group analysis of the composite was recorded by a Perkin Elmer Spectrum One FTIR spectrophotometer equipped with an Attenuated Total Reflection (ATR) accessory in the range of 4,000 to 550 cm<sup>-1</sup> with a resolution of 4 cm<sup>-1</sup>. X-ray diffraction (XRD) analysis was carried out using a PAN analytical X'pert PRO diffractometer. The samples were put on a flat plate, and the intensity data were obtained as a function of the Bragg angle in the range  $2\theta = 10^{\circ}-90^{\circ}$  with a step size of 0.013°. Elemental analysis of g-C<sub>3</sub>N<sub>4</sub>/Fe<sub>3</sub>O<sub>4</sub> composite was performed using a CHNS analyzer by Thermo Scientific, Flash 2000. The surface morphology was analyzed using a Benchtop Field Emission Scanning Electron Microscope (FESEM) (Phenom XL), while Zeta potential was measured on Malvern Instrument/ (Nano ZS/UK). A vibrating sample magnetometer (VSM, model 7404, Lake Shore, McCourkle Boulevard, WO, USA) was utilized to examine the magnetic properties of the adsorbent at room temperature. The pH at the point of zero charges (pH<sub>pzc</sub>) was determined using the salt addition method. This involved adding 0.10 g of g-C<sub>3</sub>N<sub>4</sub>/Fe<sub>3</sub>O<sub>4</sub> to 50 mL of 0.1 N sodium chloride (NaCl) electrolyte, buffered to pH 2.00-12.00 with HCl or NaOH. After 24 hours of stirring at room temperature, the pH difference was measured to establish the p $H_{pzc}$  of g- $C_3N_4/Fe_3O_4$ .

#### **Batch adsorption studies**

The adsorption studies were performed in triplicate by introducing 40 mg of g-C<sub>3</sub>N<sub>4</sub>/Fe<sub>3</sub>O<sub>4</sub> into 50 mL of methylene blue solutions with concentrations ranging from 10 to 300 mg/L. The mixture was stirred on an orbital shaker at 100 rpm for 1 hour at 298K to ensure a thorough interaction. Kinetic studies were conducted by varying contact times from 10 to 360 minutes at a fixed concentration of 50 mg/L at 298K. The effect of temperature was investigated by subjecting the solution to variation temperature from 298K to 328K. The pH effect was studied by adjusting the pH solutions using HCl or NaOH. The supernatant of the reaction mixture was separated using filter paper, and the concentration of methylene blue in the filtrate was quantified using a UV-visible spectrophotometer (Thermo Spectronic). percentage removal (%) and adsorption capacity of composite (q<sub>e</sub>, mg/mg) were determined using Equation (1) and (2), respectively:

Removal (%) = 
$$\frac{(C_0 - C_e)}{C_o} \times 100$$
 (1)

$$q_e = \frac{(C_0 \cdot C_e)}{m} V \tag{2}$$

where  $q_e$  is the mg of MB absorbed per g of g-C<sub>3</sub>N<sub>4</sub>/Fe<sub>3</sub>O<sub>4</sub> (mg/g),  $C_0$ (mg/L) is the initial MB concentration,  $C_e$ (mg/L) is the final MB concentration, V (L) is the volume of the solution,

and m is the mass of the g-C<sub>3</sub>N<sub>4</sub>/Fe<sub>3</sub>O<sub>4</sub> (g) in the reaction mixture.

# Results and Discussion Characterization of samples

Figures 1 and 2 show the FTIR spectra of the different samples. Figure 1 demonstrates the FTIR spectra of the synthesized g-C<sub>3</sub>N<sub>4</sub> through the thermal polymerization of urea. The broad bonds that appeared in the region from 3000 to 3650 cm<sup>-1</sup> were associated with the stretching vibrations of the hydroxyls (O-H) of adsorbed water and uncondensed terminal amino groups  $-NH_2$  or = NH of the g-C<sub>3</sub>N<sub>4</sub> aromatic rings [38, 39]. The peaks in the 1200-1650 cm<sup>-1</sup> range are linked to the stretching vibration of CN heterocyclic compounds, particularly the tri-striazine ring and the imine (C=N) group [40]. The heptazine ring's out-of-plane bending vibrations are represented by the peaks at 1245 and 1322 cm<sup>-1</sup> [41]. Additionally, the less intense peaks at 812 cm<sup>-1</sup> correspond to the breathing mode of tri-s-triazine, a six-membered heterocyclic ring that is present in the g-C<sub>3</sub>N<sub>4</sub> structure, while the peak at 890 cm<sup>-1</sup> is ascribed to the N-H bonds deformed in a cross-linked manner [40]. Meanwhile, **Figure 2** shows the FTIR spectra of g-C<sub>3</sub>N<sub>4</sub>/Fe<sub>3</sub>O<sub>4</sub> before and after the adsorption of MB. The emergence of additional peaks at 501 cm<sup>-1</sup> in the FTIR spectra of g-C<sub>3</sub>N<sub>4</sub>/Fe<sub>3</sub>O<sub>4</sub> indicates the stretching vibration of Fe-O in Fe<sub>3</sub>O<sub>4</sub>, confirming the successful introduction of iron particles into the g-C<sub>3</sub>N<sub>4</sub>/Fe<sub>3</sub>O<sub>4</sub> [42]. It is important to note that the main characteristic peaks of all prepared samples in Figures 1 and 2 were similar. This suggests that the chemical structure of the g-C<sub>3</sub>N<sub>4</sub> framework was retained even after iron incorporation (see Figure 2). It is also noteworthy that even with the adsorption of MB, no impurity peaks were found, and the characteristic peaks of g-

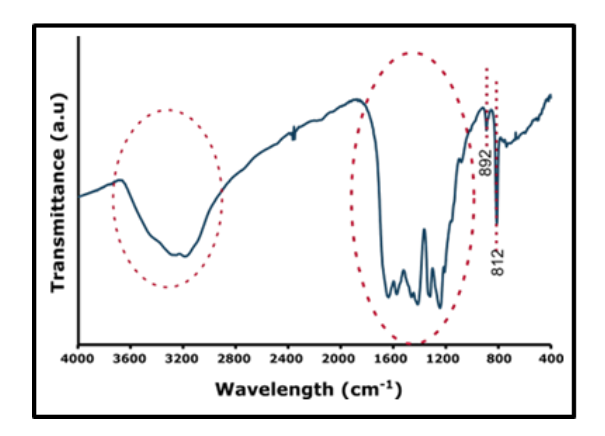
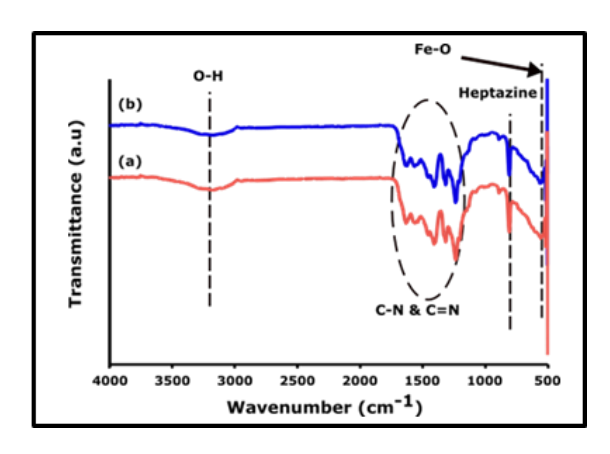


Figure 1. FTIR spectra of g-C<sub>3</sub>N<sub>4</sub>

 $C_3N_4/Fe_3O_4$  did not shift, indicating that they did not alter the initial network structure of pure g- $C_3N_4$  materials (see **Figure 2**). All the prepared samples exhibited almost identical spectra at around 1200 to  $1650 \text{ cm}^{-1}$ ,  $890 \text{ cm}^{-1}$ ,  $812 \text{ cm}^{-1}$ , and broadband at  $3000 \text{ to } 3650 \text{ cm}^{-1}$ , indicating the presence of the g- $C_3N_4$ .

Figure 3 displays the XRD diffractogram of g-C<sub>3</sub>N<sub>4</sub>, Fe<sub>3</sub>O<sub>4</sub>, and g-C<sub>3</sub>N<sub>4</sub>/Fe<sub>3</sub>O<sub>4</sub>. The dominant and strong p eak was detected at approximately  $2\theta = 27.6^{\circ}$ , corres ponding to the (002) plane of g-C<sub>3</sub>N<sub>4</sub> (JCPDS 87-152 6) (see **Figure 3 (a)**), indicating the stacking of the c onjugated aromatic system of g-C<sub>3</sub>N<sub>4</sub> [43]. The small peak at about  $2\theta = 13.4^{\circ}$  that is assigned to the (100) plane (JCPDS 87-1526), is attributed to the interlayer stacking of the tri-s-triazine motif's in-plane nitrogen connections [44, 45]. These findings support the succ essful synthesis of g-C<sub>3</sub>N<sub>4</sub> through the thermal polym erization of urea, as the observed peaks are in good a greement with the characteristic crystalline structure of g-C<sub>3</sub>N<sub>4</sub>. Additionally, the purity of the synthesized g-C<sub>3</sub>N<sub>4</sub> was confirmed by the absence of impurities i n the XRD pattern. The XRD diffractogram of Fe<sub>3</sub>O<sub>4</sub> in **Figure 3** (b) indicates that it is the crystalline phas e of Fe<sub>3</sub>O<sub>4</sub>, with six distinctive diffraction peaks at 2θ planes of (220) at 30.7°, (311) at 35.7°, (400) at 43.7 °, (422) at 53.3°, (511) at 57.4° and (440) at 63.3° [34 , 46]. Samples were structured in a cubic form with a n Fd3ms space group. All the diffraction peaks agree d with JCPDS file No.19-0629. No other notable pea ks were observed, which indicates that the sample of Fe<sub>3</sub>O<sub>4</sub> is pure. The diffraction peaks observed at  $2\theta =$  $35.7^{\circ}$ ,  $43.6^{\circ}$ ,  $57.5^{\circ}$ , and  $63.2^{\circ}$  in the g-C<sub>3</sub>N<sub>4</sub>/Fe<sub>3</sub>O<sub>4</sub> co mposites correspond to the face-centered cubic spinel structure of Fe<sub>3</sub>O<sub>4</sub> deposited on g-C<sub>3</sub>N<sub>4</sub> (see Figure 3 (c)).



**Figure 2.** FTIR spectra of g-C<sub>3</sub>N<sub>4</sub>/Fe<sub>3</sub>O<sub>4</sub> composite (a) before and (b) after removal of MB from an aqueous solution

Since no additional diffraction peaks exist, the synthesized material is a combination of pure iron oxide and g-C<sub>3</sub>N<sub>4</sub> [47]. The XRD results demonstrated a decrease in intensity, and broadening of the peaks corresponding to the (100) and (002) planes of g-C<sub>3</sub>N<sub>4</sub>, along with an increase in lattice spacing of the (002) peak, suggesting a close interaction between Fe<sub>3</sub>O<sub>4</sub> nanoparticles and g-C<sub>3</sub>N<sub>4</sub>, impeding the growth of graphitic carbon nitride crystals. Consequently, the growing environment changes, leading to the formation of Fe<sub>3</sub>O<sub>4</sub>/g-C<sub>3</sub>N<sub>4</sub> composites. This interaction leads to the formation of g-C<sub>3</sub>N<sub>4</sub>/Fe<sub>3</sub>O<sub>4</sub> composites, as confirmed by the characteristic peaks of both materials in the XRD diffractogram.

Table 1 shows that all samples, apart from carbon and nitrogen, also had a small quantity of hydrogen. It is evident that the g-C<sub>3</sub>N<sub>4</sub> sample is a compound of carbon and nitrogen elements [5]. There could also be some minimal amounts of hydrogen and oxygen that come from the leftover unreacted amino group and absorbed water present in the sample [48]. This finding aligns with the observation that g-C<sub>3</sub>N<sub>4</sub> is stable in various solvents, including water, which suggests the potential for hydrogen and oxygen incorporation from the environment [49]. The g-C<sub>3</sub>N<sub>4</sub>/Fe<sub>3</sub>O<sub>4</sub> composite contains lower amounts of C, N, and H elements, particularly the C content. This further confirms the presence of Fe<sub>3</sub>O<sub>4</sub> in the composite, which was verified from XRD and FTIR. Field Electron Scanning Electron Microscopy (FESEM) analysis was used to investigate the

morphology and surface topography of the samples. The microstructure analysis of g-C<sub>3</sub>N<sub>4</sub>, Fe<sub>3</sub>O<sub>4</sub>, and g-C<sub>3</sub>N<sub>4</sub>/Fe<sub>3</sub>O<sub>4</sub> reveals distinct surface characteristics and interactions. The distinct fold-shaped structural properties and a porous nature with the smooth surface of g-C<sub>3</sub>N<sub>4</sub> are observed in **Figure 4 (a)**. Meanwhile, Fe<sub>3</sub>O<sub>4</sub> nanoparticles exhibited a smoother surface compared to g-C<sub>3</sub>N<sub>4</sub>, with the absence of particles on the Fe<sub>3</sub>O surface indicating the absence of other residuals (**Figure 4 (b)**). However, the microstructure of g-C<sub>3</sub>N<sub>4</sub>/Fe<sub>3</sub>O<sub>4</sub> exhibits an irregular granule appearance with more rough surfaces, suggesting the presence of iron oxide particles distributed on the surface of g-C<sub>3</sub>N<sub>4</sub> surface (**Figure 4 (c)**).

Figure 5 illustrates the magnetic properties of Fe<sub>3</sub>O<sub>4</sub> nanoparticles and g-C<sub>3</sub>N<sub>4</sub>/Fe<sub>3</sub>O<sub>4</sub> composite at room temperature. The results reveal that the Fe<sub>3</sub>O<sub>4</sub> nanoparticles and g-C<sub>3</sub>N<sub>4</sub>/Fe<sub>3</sub>O<sub>4</sub> composite have the maximum saturation magnetization value of 90 emu/g and 33.00 emu/g, respectively. This value confirms the composite exceptional magnetic capabilities that enable it to be separated from the solution by using an external magnet. The reduction in magnetic behavior can be attributed to the presence of nonmagnetic g-C<sub>3</sub>N<sub>4</sub> that acts as a barrier, impeding the magnetic properties of Fe<sub>3</sub>O<sub>4</sub> nanoparticles thereby reducing the overall magnetic behavior of the sample. Apart from that, there is no hysteresis, remanence, or coercivity in the magnetic hysteresis loops, indicating that the samples are superparamagnetic.

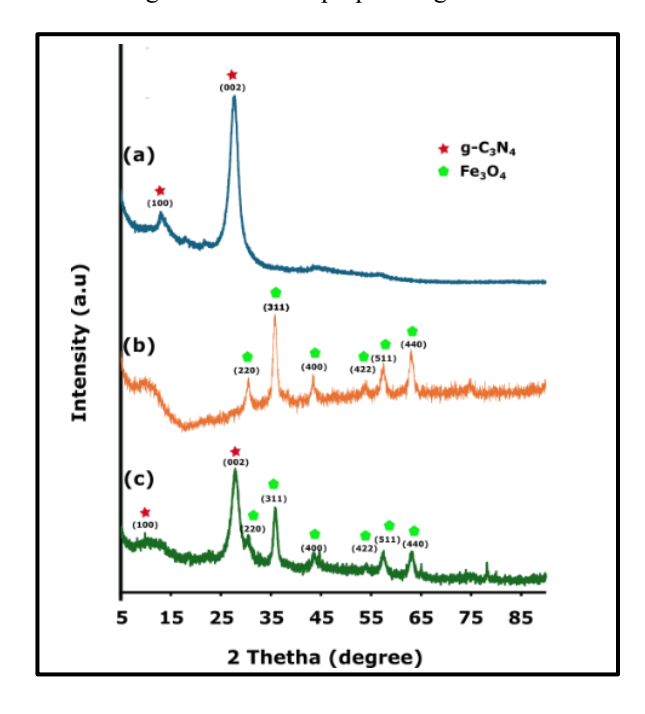


Figure 3. XRD diffractogram of the (a) g-C<sub>3</sub>N<sub>4</sub>, (b) Fe<sub>3</sub>O<sub>4</sub>, and (c) g-C<sub>3</sub>N<sub>4</sub>/Fe<sub>3</sub>O<sub>4</sub>.

Malays. J. Anal. Sci. Volume 29 Number 2 (2025): 1340

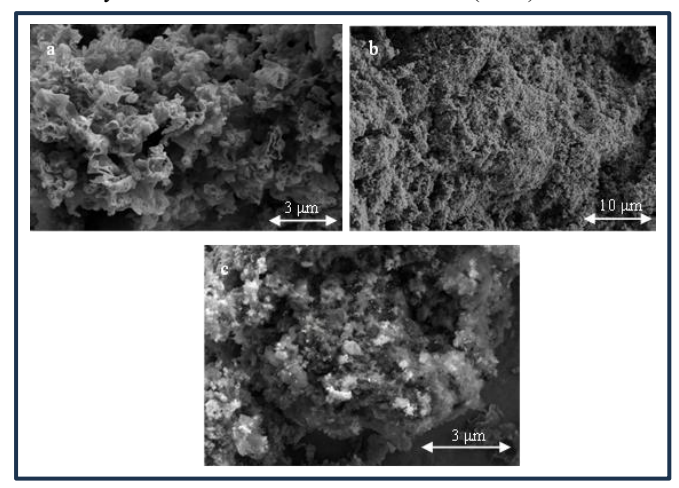


Figure 4. FESEM micrographs of (a) g-C<sub>3</sub>N<sub>4</sub>, (b)/Fe<sub>3</sub>O<sub>4</sub>, and g-C<sub>3</sub>N<sub>4</sub>/Fe<sub>3</sub>O<sub>4</sub>

**Table 1.** Elemental analysis of all samples

Sample	Nitrogen (%)	Carbon (%)	Hydrogen (%)	Oxygen (%)
g-C <sub>3</sub> N <sub>4</sub>	65.63	32.73	1.64	0
Fe <sub>3</sub> O <sub>4</sub>	0.0000	2.26	0.51	97.23
$g-C_3N_4/Fe_3O_4$	58.14	27.56	1.56	12.74

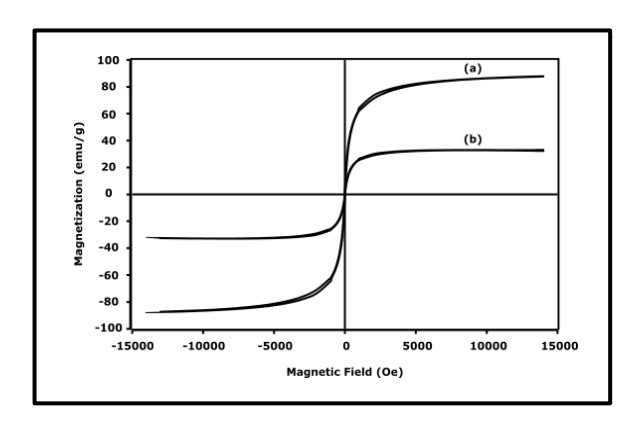


Figure 5. Magnetization curves of (a) Fe<sub>3</sub>O<sub>4</sub> and (b) g-C<sub>3</sub>N<sub>4</sub>/Fe<sub>3</sub>O<sub>4</sub>

# **Adsorption studies**

The pH of the solution is essential for determining the chemical speciation of MB in sorbents, the surface charge of the adsorbent, and the ionization of functional groups present on the surface. **Figure 6a** shows the effect of pH on the adsorption of MB on g-C<sub>3</sub>N<sub>4</sub>/Fe<sub>3</sub>O<sub>4</sub> composite. According to the findings, the adsorption of MB onto the composite gradually increases as the solution pH rises until reaching pH 5.0. At that point, subsequent increases in pH values showed slight declines until pH 8.0. The removal percentage exhibits an upward trend, rising from 9.62% at pH 2.0 to 46.03% at pH 5.0, followed by a decline to 36.99% at pH 8.0. Under extremely acidic conditions, the functional groups on the adsorbent surface become protonated, reducing or eliminating

their negative charge. This leads to weakened or repulsive electrostatic interactions with the positively charged methylene blue (MB) molecules, hindering their adsorption onto the surface [50]. The presence of proton ions (H+) occupying the active sites on the surface prevents methylene blue (MB) from binding effectively to these sites [51]. The limited adsorption can be attributed to the competition between MB and the significant mobility of H<sub>3</sub>O<sup>+</sup> ions, which effectively compete for available adsorption sites. Consequently, adsorption efficiency decreases under acidic conditions due to reduced adsorption at low pH levels. However, as the pH increases, the concentration of H<sup>+</sup> ions decrease, allowing the MB to more effectively reach the adsorption sites with less competition, resulting in increased removal of MB. Also, in a basic environment, negatively charged sites increase, promoting electrostatic attraction and enhancing adsorption [52]. As the pH solution increases, the functional groups become more ionized and deprotonated, resulting in a negative charge on these functional groups. This negative charge facilitates the attraction of positively charged MB molecules through electrostatic interactions, leading to an increase in the adsorption rate [42]. Further increasing of pH beyond 5 may be due to the saturation site of the adsorbent, making the MB unable to adsorb more on the surface of the adsorbent.

The kinetic studies conducted on g-C<sub>3</sub>N<sub>4</sub>/Fe<sub>3</sub>O<sub>4</sub> for the removal of methylene blue (MB) provided valuable insights into the adsorption process. The investigation was carried out over 360 minutes at 298 K, pH 5.0, with an initial MB concentration of 50 mg/L. The effect of time on the percentage removal of MB is depicted in Figure 6b. According to the results in Figure 6b, the adsorption of MB increased from 48.28% at 10 minutes to 57.78% at 360 minutes, with the maximum uptake achieved at the end of the experiment. Initially, the rapid adsorption of MB was attributed to the abundance of vacant surface sites on g-C<sub>3</sub>N<sub>4</sub>/Fe<sub>3</sub>O<sub>4</sub>, which gradually became occupied by MB molecules, leading to a repulsive force between the surface and MB. The large number of initially available unoccupied adsorption sites on the g-C<sub>3</sub>N<sub>4</sub>/Fe<sub>3</sub>O<sub>4</sub> surface, and it was gradually occupied until saturation was reached, that is explained by the increase in MB uptake [53]. However, a prolonged exposure beyond the optimum time hindered an effective MB removal due to the decrease in available adsorption sites and the accumulation of metal ion species, inhibit the diffusion of MB onto the surface and subsequently reducing the adsorption rate. As a result, the rate uptake of metal ion decreases that also lowers on the adsorption percentage [16].

**Figure 6c** illustrates the percentage of MB removed f rom an aqueous solution at various initial concentrati ons ranging from 10 to 300 mg/L over a contact time of 1 hour. It demonstrates a clear trend where an increase in the initial concentration of MB leads to a decrease in the percentage removal of the dye. Specificall y, the highest percentage removal of 81.11% was ach ieved at the concentration of 10 mg/L, and eventually begins to decline its percentage removal to 6.31% at 300 mg/L. This decline in removal efficiency with in

creasing initial concentration can be attributed to the phenomenon where, at lower concentrations, there is a greater extent of adsorption due to the greater avail ability of binding sites, leading to a more effective re moval. However, as the concentration increases, ther e is an increased competition for adsorption sites, res ulting in the saturation of these sites, and leaving mor e MB ions unabsorbed in the solution [17]. A study b y Bahrami et al. (2024) supports this trend [54]. They observed a decreased MB adsorption onto polyethyle ne microplastics with increasing dye concentrations. It is observed that the removal efficiency decreased when the initial MB concentration increased from 1 to 10 mg/L. However, it reached a peak value of 72.35% at an initial concentration of 20 mg/L and started to decrease at 60 mg/L. In contrast, Cai et al. ( 2020) reported an opposite trend, where the adsorptio n of MB onto a magnetic material increased with hig her initial concentrations of the dye [55]. This discre pancy in results highlights the complexity of adsorpti on processes and the need to consider the specific ch aracteristics of the adsorbent and the dye interaction.

An experiment was conducted to examine the impact of temperature on the removal of MB within the rang e of 298 to 328 K using a concentration of 50 mg/L o f MB and 40 mg of g-C<sub>3</sub>N<sub>4</sub>/Fe<sub>3</sub>O<sub>4</sub>. The contact period was set at 1 hour, and the pH level was maintained at 5.0. Figure 6d shows that the percentage of MB rem oval increased from 40.78% at 298 K to 45.38% at 3 28 K, indicating an endothermic adsorption process. The strong attractive forces between MB and the g-C <sub>3</sub>N<sub>4</sub>/Fe<sub>3</sub>O<sub>4</sub> at an elevated temperature contribute to thi s phenomenon [56]. High temperatures can enhance t he kinetic energy of the dye molecules and the adsor bent surface, leading to more significant molecular m ovements and collisions, which can facilitate the ads orption process. Additionally, the increase in tempera ture can lead to a decrease in solution viscosity, prom oting a faster diffusion of the dye molecules towards the adsorbent surface and into the pores, thereby enh ancing the adsorption rate [57]. The endothermic pro perties removal of MB from aqueous solution was re ported similarly using modified g-C<sub>3</sub>N<sub>4</sub> materials [58, 59]. Farhadi and Keramati (2023) [58] reveal that the positive values of  $\Delta H^{\circ}$  for both composites (g-C<sub>3</sub>N<sub>4</sub>/CP and Ex.g-C<sub>3</sub>N<sub>4</sub>/CP) indicate that the adsorption of MB is endothermic. Similar findings were obtained by Kuan et al. (2022) [59] The adsorption of MO dye onto the Ag-doped biochar/g-C<sub>3</sub>N<sub>4</sub>/TiO<sub>2</sub> was endothermic.

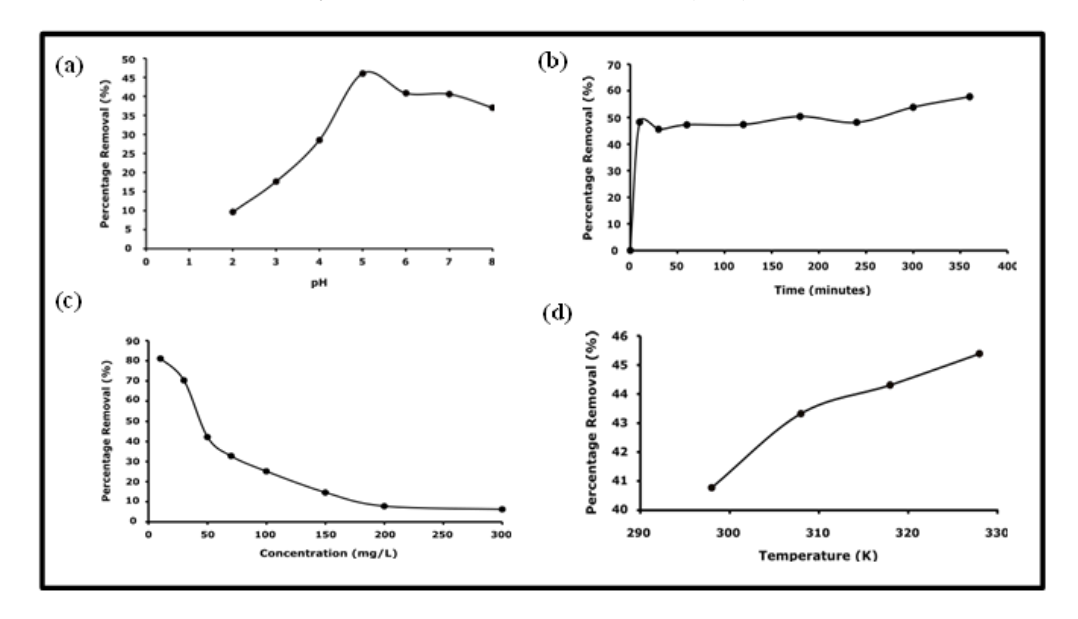


Figure 6. Effect of (a) pH, (b) contact time, (c) initial concentration, and (d) temperature on the MB adsorption onto g-C<sub>3</sub>N<sub>4</sub>/Fe<sub>3</sub>O<sub>4</sub>

#### Thermodynamic properties

The thermodynamic parameters, including  $\Delta G^{\circ}$ (standard Gibbs free energy change), ΔH° (standard enthalpy change), and  $\Delta S^{\circ}$  (standard entropy change) for MB adsorption, were calculated using experimental data collected at different temperatures. Those parameters are crucial in determining the spontaneity and the nature of the adsorption process. The standard free energy change ( $\Delta G^{\circ}$ ), enthalpy change ( $\Delta H^{\circ}$ ), and entropy change ( $\Delta S^{\circ}$ ) are typically determined using Eqs. (3) and (4):

$$k_{d} = \frac{q_{e}}{C_{e}}$$

$$\ln k_{d} = -\frac{\Delta G^{\circ}}{RT} = \frac{\Delta S^{\circ}}{R} - \frac{\Delta H^{\circ}}{T}$$
(4)

$$\ln k_{\rm d} = -\frac{\Delta G}{RT} = \frac{\Delta S}{R} - \frac{\Delta H}{T} \tag{4}$$

where  $k_{\text{d}}$  is the distribution coefficient,  $q_{\text{e}}$  is the concentration of MB adsorbed onto g-C<sub>3</sub>N<sub>4</sub>/Fe<sub>3</sub>O<sub>4</sub> at equilibrium (mg/L), C<sub>e</sub> is the equilibrium concentration of MB in the liquid phase (mg/L), R is the universal gas constant (8.314 J/mol K), and T is the absolute temperature (K). The Van't Hoff plot (Ink<sub>d</sub> vs. 1/T) was used to compute the values of  $\Delta H^{\circ}$ 

and  $\Delta S^{\circ}$ . These values were obtained from the slope and intercept, displayed in Table 2 below.

The positive  $\Delta G^{\circ}$  values imply that it is a nonspontaneous adsorption process, aligned with the study's findings [60, 61]. The decrease in  $\Delta G^{\circ}$  as the temperature rises indicates enhanced adsorption at higher temperatures, suggesting a temperaturedependent effect on adsorption [60, 62]. However, the negative values of  $\Delta G^{\circ}$  at 328 K (-0.104 kJ/mol) signified a spontaneous adsorption process, possibly due to accessible active sites on the adsorbent surface or increased mobility of dye molecules in solution at higher temperatures [63, 64]. The positive  $\Delta H^{\circ}$  value of 4.94 kJ/mol for g-C<sub>3</sub>N<sub>4</sub>/Fe<sub>3</sub>O<sub>4</sub> materials indicates that the adsorption of MB onto g-C<sub>3</sub>N<sub>4</sub>/Fe<sub>3</sub>O<sub>4</sub> signifies an endothermic process. This confirms that physical forces are primarily involved in the adsorption mechanism, which aligns with reducing the amount of MB adsorbed at higher temperatures. The positive value of  $\Delta S^{\circ}$  indicates an increase in disorder at the border between the solid and solution interface during adsorption.

**Table 2.** Thermodynamic parameters for the adsorption of MB by g-C<sub>3</sub>N<sub>4</sub>/Fe<sub>3</sub>O<sub>4</sub>

Temperature (K)	ΔG <sup>O</sup> (kJ/mol)	ΔH <sup>O</sup> (kJ/mol)	ΔS <sup>O</sup> (J/mol K)
298	0.372	4.94	15.46
308	0.116		
318	0.014		
328	-0.104		

The positive entropy value means that the adsorption process increases the degree of freedom and disorder, which is consistent with an endothermic process. This phenomenon implies that the adsorption process becomes more favourable with an increasing temperature, as it enhances the randomness and affinity of the adsorbents for the dye.

### Adsorption isotherm studies

Adsorption models are essential for understanding the adsorption process by providing insights into the adsorbate-adsorbent interaction. Langmuir and Freundlich's models are commonly used to analyze the adsorption equilibrium data and explore the interaction between MB and g-C<sub>3</sub>N<sub>4</sub>/Fe<sub>3</sub>O<sub>4</sub>. It also helps determine essential parameters that govern the adsorption behaviour of the system under investigation. **Figure 7** illustrates the linear isotherm models for MB's adsorption onto g-C<sub>3</sub>N<sub>4</sub>/Fe<sub>3</sub>O<sub>4</sub>. Additionally, **Table 3** provides estimated isotherm parameters, offering quantitative insights into the adsorption process and the characteristics of the interaction between adsorbate and adsorbent.

Langmuir's model proposes a monolayer adsorption on a homogeneous surface with an unlimited number of adsorption sites and negligible molecular interactions. It explains monolayer adsorption by dye molecules covering the active sites that prevent further adsorption. The saturated monolayer isotherm of the Langmuir model is expressed as follows [64]:

$$\frac{C_e}{q_e} = \frac{1}{K_L q_{max}} + \frac{C_e}{q_{max}}$$
 (5)

where  $q_e$  is the quantity of MB adsorbed at equilibrium (mg/g),  $C_e$  is the concentration of MB at equilibrium (mg/L),  $q_{max}$  (mg/g) is the maximum MB adsorption (mg/g) when all adsorptive sites are fully covered, and  $K_L$  (L/mg) is the Langmuir constant related to the energy of adsorption. The intercept and

slope of the straight line of  ${^{\rm C}_{\rm e}}/{\rm q_{\rm e}}$  vs.  ${\rm C_{\rm e}}$  (**Figure 7** (a)) can be used to get the values of b and  ${\rm q_{\rm max}}$ .

On the other hand, the Freundlich model assumes multilayer adsorption on heterogeneous surfaces with varying adsorption energies. Furthermore, the adsorbed molecules have the capacity to interact with one another. The Freundlich isotherm equation can be expressed in a linear form as [16, 17, 65]:

$$\ln q_e = \ln K_f = \frac{1}{n_F} \ln C_e \tag{6}$$

where  $q_e$  is the equilibrium amount of MB adsorbed (mg/g) and  $C_e$  is the equilibrium concentration of MB in the aqueous phase (mg/L). The  $n_F$  value reflects the adsorption favorability; if  $n_F > 1$  indicates a favourable adsorption, and  $K_F$  (mg/g) is the Freundlich constant related to adsorption capacity. The intercept and slope of the plot  $\ln q_e$  vs.  $\ln C_e$  shown in **Figure 7(b)** can be utilized to compute the  $K_F$  and  $n_F$ .

In the case of MB adsorption onto g-C<sub>3</sub>N<sub>4</sub>/Fe<sub>3</sub>O<sub>4</sub>, the Langmuir model was found to provide a better fit to the experimental data compared to the Freundlich model, as indicated by the higher  $R^2$  value. The Langmuir isotherm model suggests that the adsorption process of Methylene Blue (MB) onto g-C<sub>3</sub>N<sub>4</sub>/Fe<sub>3</sub>O<sub>4</sub> occurs on a homogeneous surface with uniform adsorption binding sites. This indicates that each MB molecule interacts with the adsorbent surface with the same adsorption activation energy [65, 66]. The results further show that the adsorption occurs in the form of monolayer coverage onto the homogeneous surface of the g-C<sub>3</sub>N<sub>4</sub>/Fe<sub>3</sub>O<sub>4</sub>. The calculated monolayer capacity (q<sub>max</sub>) of MB (40.2 mg/g) adsorbed onto g-C<sub>3</sub>N<sub>4</sub>/Fe<sub>3</sub>O<sub>4</sub> closely aligns with the maximum experimental adsorption capacity observed, which was 41.80 mg/g.

Table 3. Adsorption isotherm parameter values for the adsorption of methylene blue onto g-C<sub>3</sub>N<sub>4</sub>/Fe<sub>3</sub>O<sub>4</sub>

Isotherm Model	Estimated Isotherm Parameters		
Langmuir	q <sub>max</sub> (mg/g)	40.2	
	b (L/mg)	0.529	
	$R^2$	0.997	
Freundlich	$K_F(L/g)$	15.4	
	$n_{\mathrm{F}}$	5.00	
	$R^2$	0.612	

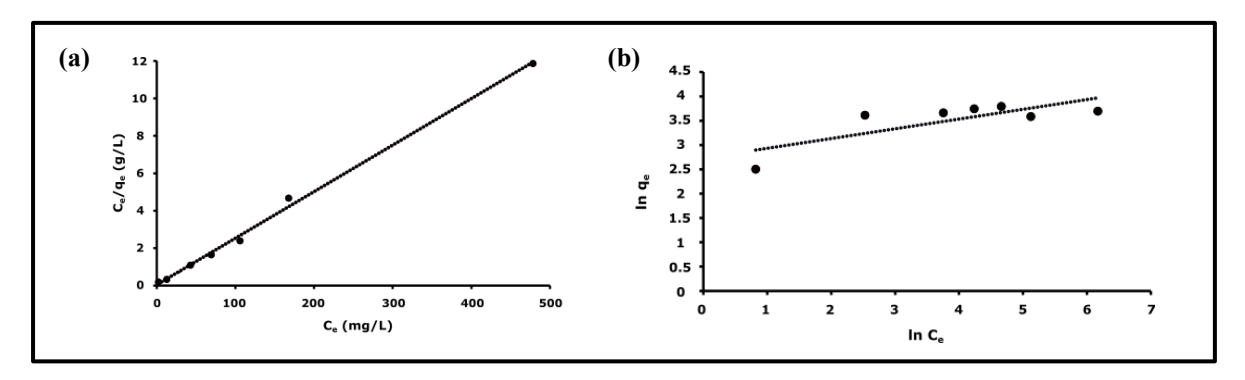


Figure 7. (a) Langmuir and (b) Freundlich plots for the adsorption of methylene blue onto g-C<sub>3</sub>N<sub>4</sub>/Fe<sub>3</sub>O<sub>4</sub>

The dimensionless equilibrium parameter  $R_L$ , was used to interpret the Langmuir isotherm properties and is defined as:

$$R_{L} = \frac{1}{1 + bC_{o}} \tag{7}$$

The R<sub>L</sub> values obtained for adsorption onto the g-C<sub>3</sub>N<sub>4</sub>/Fe<sub>3</sub>O<sub>4</sub> indicated a favourable adsorption behaviour, with decreasing R<sub>I</sub> values at higher concentrations suggesting an enhanced adsorption at higher initial MB concentrations [67]. According to **Table 3**, the Freundlich isotherm shows that  $n_E$ values are greater than 1, and 1/n<sub>F</sub> values are less than 1 for the MB adsorption system. This suggests that both physical adsorption and the normal Langmuir isotherm are favorable. It appears that there may be a correlation between the distribution of surface sites and the strength of the interaction between the adsorbent and adsorbate. This relationship seems to weaken as the surface density increases [68]. Nevertheless, the correlation coefficient was less than 0.99, suggesting that the Freundlich model was not appropriate for the present study.

# Adsorption kinetics studies

Understanding the contact time is crucial when studying adsorption kinetics, as it has a significant influence on the effectiveness of adsorption. Pseudofirst-order and pseudo-second-order models were utilized to access the adsorption of MB on g-C<sub>3</sub>N<sub>4</sub>/Fe<sub>3</sub>O<sub>4</sub>. The coefficients for linear regression, R<sup>2</sup>, and the parameters for the pseudo-first-order and pseudo-second-order kinetic models can be found in **Table 4.** 

The equation represents the pseudo-first-order rate is expressed as [16]:

$$\log(q_e - q_t) = \log q_e - \frac{k_1}{2.303}t$$
 (8)

The equation represents the pseudo-second-order is shown as [16]:

$$\frac{t}{q_{t}} = \frac{1}{k_{2}q_{e}^{2}} + \frac{t}{q_{e}} \tag{9}$$

where  $q_t$  is the quantity of MB adsorbed at contact time t (mg/g),  $q_e$  is the amount of MB adsorbed per unit sorbent mass at equilibrium (mg/g).  $k_1$  and  $k_2$  are the pseudo-first- and pseudo-second-order reaction rate constants, respectively. The intercept and slope of the  $\log(q_e-q_t)$  vs. t plot can be used to calculate the value of  $k_1$  and theoretical  $q_{e, \, cal}$  values for MB adsorption. The intercept and slope of the  $t/q_t$  vs. t plot can be used to calculate the value of  $k_2$  and theoretical  $q_{e, \, cal}$  values (**Figure 8**).

**Table 4**. Kinetic parameters for the removal of methylene blue by g-C<sub>3</sub>N<sub>4</sub>/Fe<sub>3</sub>O<sub>4</sub>

Pseudo-first-order			Pseudo-second-order				
$q_{e \ exp} \ ( ext{mg/g})$	k <sub>1</sub> (Min <sup>-1</sup> )	q <sub>e, cal</sub> (mg/g)	$R^2$	k <sub>2</sub> (g/mg min)	q <sub>e cal</sub> (mg/g)	h	$R^2$
57.3	0.001	15.4	0.659	0.01	55.6	4.18	0.987

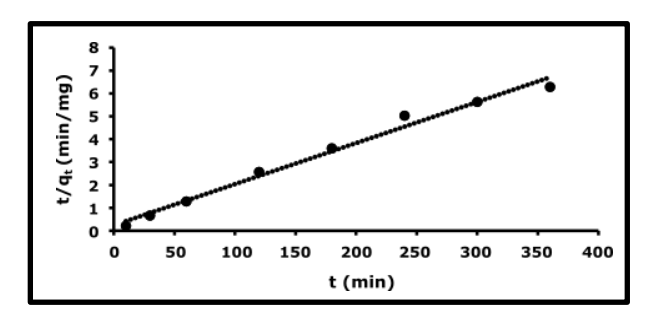


Figure 8. Pseudo-second-order kinetics for the MB adsorption onto g-C<sub>3</sub>N<sub>4</sub>/Fe<sub>3</sub>O

The parameters of the pseudo-first-order and pseudo-second-order kinetic models, along with the linear regression coefficient,  $(R^2)$ , are presented in **Table 4.** It was noted that the pseudo-first-order model was not suitable because of a low reaction constant  $(k_1)$ , and very weak correlation  $(R^2)$  together with the differences between the measured  $q_e$  values and the experimental  $q_e$  value. This suggests that the dye's adsorption did not happen through physisorption. The correlation coefficients  $(R^2)$  for the pseudo-first-order and pseudo-second-order models were found to be 0.659 and 0.987, respectively, as indicated in **Table 4.** 

The higher R<sup>2</sup> values for the pseudo-second-order model indicated a better correlation with the experimental data, suggesting that the adsorption process followed the pseudo-second-order kinetic model more closely than the pseudo-first-order model. Moreover, the calculated q value using the pseudo-second-order model was closer to the experimental  $q_e$  value, providing evidence for the dominance of the pseudo-second-order kinetic model. The evidence points to chemisorption, rather than boundary layer resistance, as the likely ratedetermining step that limits the adsorption process onto g-C<sub>3</sub>N<sub>4</sub>/Fe<sub>3</sub>O<sub>4</sub>. This implies that the rate of MB dye adsorption is dependent on the total number of active sites available for the g-C<sub>3</sub>N<sub>4</sub>/Fe<sub>3</sub>O<sub>4</sub> material to act upon. The findings align with the concept that the adsorption process is more influenced by chemical interactions at the surface rather than mass transfer limitations at the boundary layer.

# Mechanistic insights into adsorption

Understanding the process of adsorption better requires examining adsorbent preparation and adsorption mechanisms, which can help develop adsorption systems for various applications in the future. Figure 9 depicts the possible adsorption mechanism of g-C<sub>3</sub>N<sub>4</sub>/Fe<sub>3</sub>O<sub>4</sub>. The determined pH<sub>pzc</sub> of g-C<sub>3</sub>N<sub>4</sub>/Fe<sub>3</sub>O<sub>4</sub> was 4.20 indicating the acidity of the surface characteristics. Below this pH value, the surface becomes positively charged due to protonation, favouring anion adsorption, while above the pH<sub>pzc</sub>, the surface carries a negative charge, facilitating the adsorption of cation species. This phenomenon elucidates the adsorption of cationic dves onto g-C<sub>3</sub>N<sub>4</sub>/Fe<sub>3</sub>O<sub>4</sub>, involving  $\pi$ - $\pi$  conjugate interactions and electrostatic attractions. The results from **Figure 6a** suggest that the adsorption of MB is more efficient at pH 5.0, which is above the pH<sub>pzc</sub>. Electron donor-receptor relationships between MB and g-C<sub>3</sub>N<sub>4</sub>/Fe<sub>3</sub>O<sub>4</sub> structures exist in adsorption beyond interactions. Hence, all further experiments were conducted at pH 5.0 to facilitate electrostatic interactions between the MB and the g-C<sub>3</sub>N<sub>4</sub>/Fe<sub>3</sub>O<sub>4</sub> surface. It has been proposed that an electrostatic interaction (orange block) took place between MB and g-C<sub>3</sub>N<sub>4</sub>/Fe<sub>3</sub>O<sub>4</sub> due to the cationic nature of MB and the negative charge of g-C<sub>3</sub>N<sub>4</sub>/Fe<sub>3</sub>O<sub>4</sub> in the solution. Both MB and g-C<sub>3</sub>N<sub>4</sub>/Fe<sub>3</sub>O<sub>4</sub> possess aromatic rings with delocalized  $\pi$ -electrons, which may result in a potentially enhanced  $\pi$ - $\pi$  interaction (blue block). This further increased the interaction between g-C<sub>3</sub>N<sub>4</sub>/Fe<sub>3</sub>O<sub>4</sub> and MB, facilitating the removal of MB from the aqueous solutions. Furthermore, the lone pair on the nitrogen atom or hydroxyl group of g-C<sub>3</sub>N<sub>4</sub>/Fe<sub>3</sub>O<sub>4</sub> can potentially establish hydrogen bonds (purple block) with the hydrogen atom or nitrogen atom of MB, respectively. Meanwhile, the zeta potential measurements were made at room temperature for the g-C<sub>3</sub>N<sub>4</sub> and g-C<sub>3</sub>N4/Fe<sub>3</sub>O<sub>4</sub> suspensions of -16.7 mV and -21.4 mV, which is advantageous for binding cationic ions electrostatically. The analysis indicated that the adsorption of MB onto g-C<sub>3</sub>N4/Fe<sub>3</sub>O<sub>4</sub> was mainly influenced by electrostatic interactions, as well as  $\pi$ - $\pi$ interaction and hydrogen bonding.

Malays. J. Anal. Sci. Volume 29 Number 2 (2025): 1340

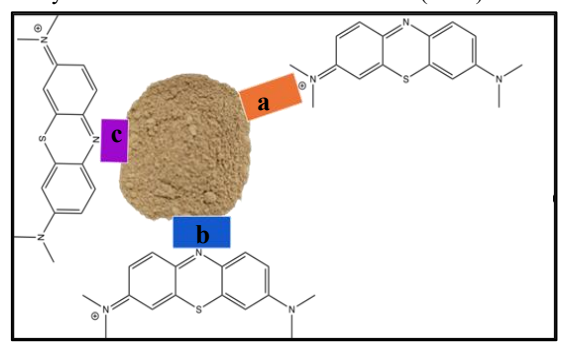


**Figure 9.** Possible adsorption mechanisms of MB onto g-C<sub>3</sub>N<sub>4</sub>/Fe<sub>3</sub>O<sub>4</sub> (brown powder) at pH =  $5.0 > pH_{PZC}$ : (a) electrostatic attraction, (b)  $\pi$ - $\pi$  interaction, and (c) hydrogen bonding

# Comparison with other adsorbents

**Table 5** shows the comparison of methylene blue adsorption capabilities  $(q_{max})$  with different adsorbents, as reported in the previous studies. The value of adsorption capacity in the present work is significantly considerable compared to most other adsorbents reported. Thus, the current work revealed that  $g-C_3N4/Fe_3O_4$  has the potential to be an effective, efficient, economical adsorbent for removing MB from aqueous solutions due to the easy separation from the solution.

### **Conclusions**

The study demonstrated the effectiveness of g-C<sub>3</sub>N<sub>4</sub>/Fe<sub>3</sub>O<sub>4</sub> in adsorbing cationic dyes, particularly methylene blue, showcasing its potential for environmental remediation applications. XRD and FTIR analyses verified the formation of g-C<sub>3</sub>N<sub>4</sub>/Fe<sub>3</sub>O<sub>4</sub> composite through the chemical coprecipitation method. The research evaluated parameters such as pH, contact time, initial concentration, and temperature to optimize the adsorption efficiency, with pH 5.0 at 50 mg/L and contact time of 1 hour being the most favorable conditions for maximum adsorption efficiency. The Langmuir isotherm model effectively represented the equilibrium data, indicating that the MB adsorption onto g-C<sub>3</sub>N<sub>4</sub>/Fe<sub>3</sub>O<sub>4</sub> followed the monolayer and adsorption processes, with a maximum adsorption capacity of 40.2 mg/g. Moreover, the pseudo-secondorder model revealed that chemical sorption was the rate-limiting step, with the adsorption rate showing a sharp rise within the first 30 minutes, followed by a plateau afterward. The thermodynamic analysis highlighted a positive Gibbs free energy value, indicating a non-spontaneous reaction, and a positive enthalpy value, suggesting an endothermic process. The comprehensive analysis of MB adsorption onto g-C<sub>3</sub>N<sub>4</sub>/Fe<sub>3</sub>O<sub>4</sub>, supported by the Langmuir isotherm model and pseudo-second-order kinetics, indicated the potential of g-C<sub>3</sub>N<sub>4</sub>/Fe<sub>3</sub>O<sub>4</sub> as an effective adsorbent for removing MB, with implications for environmental remediation applications. Although a numerous study has been done on the usage of g-C<sub>3</sub>N<sub>4</sub>/Fe<sub>3</sub>O<sub>4</sub> composites for the removal of oils, heavy metals, and pharmaceutical products, there is still a huge research gap when it comes to dye removal. The limited availability of this composite underscores the necessity for additional research into its possible applications in dye cleanup procedures. In addition to broadening the applications of g-C<sub>3</sub>N<sub>4</sub>/Fe<sub>3</sub>O<sub>4</sub>, a greater study in this field may lead to dye-contaminated improved water treatment methods. thereby tackling important an environmental issue. Further research in this area could lead to the development of advanced adsorption technologies for water treatment and environmental remediation, contributing sustainable solutions for mitigating the impact of toxic pollutants on ecosystems and human health.

**Table 5.** Comparison of adsorption capacities (mg/g) for dyes onto different adsorbent

Adsorbents	Pollutants	Adsorption Capacity (mg/g)	References
Chitosan-n SiO <sub>2</sub> nanocomposite	methylene blue	21.32–31.34	[69]
Boron-doped mesoporous carbon nitride	malachite green	54	[70]
Tetragonal C <sub>3</sub> N <sub>4</sub> hollow tubes	methylene blue	7	[71]
C-doped g-C <sub>3</sub> N <sub>4</sub>	methylene blue	58	[72]
$g-C_3N4/Fe_3O_4$	methylene blue	40.2	This work

#### Acknowledgement

We wish to extend our appreciation to the Ministry of Higher Education for financial support under the Fundamental Research Grants Scheme (FRGS/1/2023/STG05/UiTM/02/8).

#### References

- Kalia, R., A. Chauhan, R. Verma, M. Sharma, K.M. Batoo, R. Kumar, S. Hussain, S. Ghotekar, and M.F. Ijaz. (2022). Photocatalytic degradation properties of Li-Cr ions substituted CoFe<sub>2</sub>O<sub>4</sub> nanoparticles for wastewater treatment application. *Physica Status Solidi* (a), 219(8): 2100539.
- Zhai, H., Z. Liu, L. Xu, T. Liu, Y. Fan, L. Jin, R. Dong, Y. Yi, and Y. Li. (2022). Waste textile reutilization via a scalable dyeing technology: a strategy to enhance dyestuffs degradation efficiency. *Advanced Fiber Materials*, 4(6): 1595-1608.
- 3. Siregar, R.A.N., A. Sanjaya, J. Lucy, and R. Pinontoan. (2020). Methylene blue decolorizing bacteria isolated from water sewage in Yogyakarta, Indonesia. *Biodiversitas Journal of Biological Diversity*, 21(3): 1136-1141.
- Adjid, G.A.F.A., A. Kurniawan, and N. Nazriati. (2022). Textile industry waste pollution in the konto river: a comparison of public perceptions and water quality data. *The Journal of Experimental Life Science*, 12(3): 105-116.
- Lavado-Meza, C., Y. Asencios, G. Cisneros-Santos, and I. Unchupaico-Payano. (2021). Removal of methylene blue dye using Nostoc commune biomass: kinetic, equilibrium and thermodynamic study. Revista Mexicana de Ingeniería Ouímica, 20(2): 941-954.
- Li, H., X. Cao, C. Zhang, Q. Yu, Z. Zhao, X. Niu, X. Sun, Y. Liu, L. Ma, and Z. Li. (2017). Enhanced adsorptive removal of anionic and cationic dyes from single or mixed dye solutions using MOF PCN-222. RSC Advances, 7(27): 16273-16281.
- Khan, Z.U.H., N.S. Gul, F. Mehmood, S. Sabahat, N. Muhammad, A. Rahim, J. Iqbal, S. Khasim, M.A. Salam, and T.M. Khan. (2023). Green synthesis of lead oxide nanoparticles for photo-electrocatalytic and antimicrobial applications. *Frontiers in Chemistry*, 11: 75114.
- 8. Khadivi, H., M. Sirousazar, V. Abbasi-Chianeh, and E. Jalilnejad. (2022). Egg white/polyvinyl alcohol/clay bionanocomposite hydrogel adsorbents for dye removal. *Journal of Polymers and the Environment*, 30(8): 3186-3202.
- 9. Ilias, H.M., S.H. Othman, R.A. Shapi'i, and K.F.M. Yunos. (2024). Starch/chitosan nanoparticles bionanocomposite membranes for

- methylene blue dye removal. *Nanotechnology*, 35: 1361-6528.
- Alayli, A., H. Nadaroglu, and E. Turgut. (2021).
   Nanobiocatalyst beds with Fenton process for removal of methylene blue. *Applied Water Science*, 11(2): 1-8.
- 11. Pan, S., J. Shen, Z. Deng, X. Zhang, and B. Pan. (2022). Metastable nano-zirconium phosphate inside gel-type ion exchanger for enhanced removal of heavy metals. *Journal of Hazardous Materials*, 423: 127158.
- Cevallos-Mendoza, J., C.G. Amorim, J.M. Rodríguez-Díaz, and M.d.C.B. Montenegro. (2022). Removal of contaminants from water by membrane filtration: a review. *Membranes*, 12(6): 570.
- 13. Harharah, R.H., G.M. Abdalla, A. Elkhaleefa, I. Shigidi, and H.N. Harharah. (2022). a study of copper (II) ions removal by reverse osmosis under various operating conditions. *Separations*, 9(6): 155.
- 14. Jasim, M.A. and F.Y.A. AlJaberi. (2023). Treatment of oily wastewater by electrocoagulation technology: A general review (2018-2022). *Journal of Electrochemical Science and Engineering*, 13(2): 361-372.
- 15. Fan, J., S. Xue, K. Wan, G. Wang, and Z. Miao. (2023). Studies on degradation of triphenylmethane dye crystal violet by electroflotation device. *The Canadian Journal of Chemical Engineering*, 101(6): 3309-3321.
- 16. Taib, N.I., N.A. Rosli, N.I. Saharrudin, N.M. Rozi, N.A.A. Kasdiehram, and N. Nazri. (2021). Kinetic, equilibrium, and thermodynamic studies of untreated watermelon peels for removal of copper (II) from aqueous solution. *Desalination and Water Treatment*, 227: 289-299.
- 17. Tahiruddin, N.S.M., R.A. Aziz, R. Ali, and N.I. Taib. (2023). Potential of using jackfruit peel (*Artocarpus heterophyllus*) as green solution for removal of copper (II) and zinc (II) from aqueous solution: Adsorption kinetics, isotherm and thermodynamic studies. *Journal of Environmental Chemical Engineering*, 11(3): 109953.
- 18. Dutta, S., B. Gupta, S.K. Srivastava, and A.K. Gupta. (2021). Recent advances on the removal of dyes from wastewater using various adsorbents: A critical review. *Materials Advances*, 2(14): 4497-4531.
- 19. Tian, Y., Y. Yin, Z. Jia, H. Lou, and H. Zhou. (2023). One-pot preparation of magnetic nitrogen-doped porous carbon from lignin for efficient and selective adsorption of organic pollutants. *Environmental Science and Pollution Research*, 30(6): 14943-14958.

- 20. Wang, J. and S. Wang. (2022). A critical review on graphitic carbon nitride (g-C<sub>3</sub>N<sub>4</sub>)-based materials: Preparation, modification and environmental application. *Coordination Chemistry Reviews*, 453: 214338.
- 21. Azali, N.A.M., N.A. Rahman, R. Saleh, M. Mazlan, and N.I. Taib. (2023). Synthesis and characterization of the magnetically separable composite of iron oxide and graphitic carbon nitride for degradation of methylene blue. *Malaysian Journal of Chemistry*, 25(3): 64-73.
- 22. Oh, Y., J.O. Hwang, E.-S. Lee, M. Yoon, V.-D. Le, Y.-H. Kim, D.H. Kim, and S.O. Kim. (2016). Divalent Fe atom coordination in two-dimensional microporous graphitic carbon nitride. ACS Applied Materials & Interfaces, 8(38): 25438-25443.
- 23. Ahmed, A., A. Hayat, M.H. Nawaz, A.A. Chaudhry, P. John, and M. Nasir. (2021). Fluorescence quenching mediated detection of hydrogen peroxide using tungsten incorporated graphitic carbon nitride nanoflakes. *RSC Advances*, 11(13): 7479-7491.
- 24. Idris, A.O., E.O. Oseghe, T.A. Msagati, A.T. Kuvarega, U. Feleni, and B. Mamba. (2020). Graphitic carbon nitride: a highly electroactive nanomaterial for environmental and clinical sensing. *Sensors*, 20(20): 5743.
- 25. Basyach, P. and L. Saikia. (2022). Magnetic Nanoparticles Supported on g-C<sub>3</sub>N<sub>4</sub>: An efficient heterogeneous catalyst for selective transfer hydrogenation of furfural to furfuryl alcohol. *ChemistrySelect*, 7(19): e202200355.
- 26. Sewnet, A., M. Abebe, P. Asaithambi, and E. Alemayehu. (2022). Visible-light-driven g-C<sub>3</sub>N<sub>4</sub>/TiO<sub>2</sub> based heterojunction nanocomposites for photocatalytic degradation of organic dyes in wastewater: a review. *Air, Soil and Water Research*, 15: 1-23.
- 27. Li, X., B. Wang, W. Yin, J. Di, J. Xia, W. Zhu, and H. Li. (2020).  $Cu^{2+}$  modified g-C<sub>3</sub>N<sub>4</sub> photocatalysts for visible light photocatalytic properties. *Acta Physica Chimica Sinica*, 36(1902001): 10.3866.
- 28. Ragupathi, V., P. Panigrahi, and Subramaniam, N.G. (2022). Supercapacitive performance of exfoliated graphitic carbon nitride nanoflakes. IOP Conference Series: Materials Science and Engineering, 1263:12022.
- 29. Vuong, H.T., D.V. Nguyen, L.P. Phuong, P.P. Minh, B.N. Ho, and H.A. Nguyen. (2023). Nitrogen-rich graphitic carbon nitride (g-C<sub>3</sub>N<sub>5</sub>): Emerging low-bandgap materials for photocatalysis. *Carbon Neutralization*, 2(4): 425-457.
- 30. Dong, G. and L. Zhang. (2012). Porous structure dependent photoreactivity of graphitic carbon

- nitride under visible light. *Journal of Materials Chemistry*, 22(3): 1160-1166.
- 31. Sangaiya, P. and R. Jayaprakash. (2018). A review on iron oxide nanoparticles and their biomedical applications. *Journal of Superconductivity and Novel Magnetism*, 31(11): 3397-3413.
- 32. Yu, W., H. Li, L. Zhang, J. Liu, F. Kong, and W. Wang. (2020). Preparation of magnetic porous aromatic framework for rapid and efficient removal of organic pollutants from water. *Analytical Sciences*, 36(10): 1157-1161.
- 33. Chaudhari, D. and G. Panda. (2023). A brief overview on iron oxide nanoparticle synthesis, characterization, and applications. *Materials Today: Proceedings*, 10: 87.
- 34. Zambri, N.D.S., N.I. Taib, F. Abdul Latif, and Z. Mohamed. (2019). Utilization of neem leaf extract on biosynthesis of iron oxide nanoparticles. *Molecules*, 24(20): 3803.
- 35. Huo, H., X. Hu, H. Wang, J. Li, G. Xie, X. Tan, Q. Jin, D. Zhou, C. Li, and G. Qiu. (2019). Synergy of photocatalysis and adsorption for simultaneous removal of hexavalent chromium and methylene blue by g-C<sub>3</sub>N<sub>4</sub>/BiFeO<sub>3</sub>/carbon nanotubes ternary composites. *International Journal of Environmental Research and Public Health*, 16(17): 3219.
- 36. Georgiou, Y., E. Mouzourakis, A. Bourlinos, R. Zboril, M. Karakassides, A. Douvalis, T. Bakas, and Y. Deligiannakis. (2016). Surface decoration of amine-rich carbon nitride with iron nanoparticles for arsenite (III) uptake: The evolution of the Fe-phases under ambient conditions. *Journal of Hazardous Materials*, 312: 243-253.
- 37. Guo, S., K. Wu, Y. Gao, L. Liu, X. Zhu, X. Li, and F. Zhang. (2018). Efficient removal of Zn (II), Pb (II), and Cd (II) in waste water based on magnetic graphitic carbon nitride materials with enhanced adsorption capacity. *Journal of Chemical & Engineering Data*, 63(10): 3902-3912.
- 38. Alshammari, A.H., K. Alshammari, M. Alshammari, and T.A.M. Taha. (2023). Structural and optical characterization of g-C<sub>3</sub>N<sub>4</sub> nanosheet integrated PVC/PVP polymer nanocomposites. *Polymers*, 15(4): 871.
- 39. Wang, M., M. Zhang, J. Zhu, J. Wang, L. Hu, T. Sun, M. Wang, and Y. Tang. (2020). g-C<sub>3</sub>N<sub>4</sub>/Co nanohybrids for ultra-sensitive simultaneous detection of uric acid and dopamine. *ChemElectroChem*, 7(6): 1373-1377.
- 40. Waheed, I.F., M.A. Hamad, K.A. Jasim, and A.J. Gesquiere. (2023). Degradation of methylene blue using a novel magnetic CuNiFe<sub>2</sub>O<sub>4</sub>/g-C<sub>3</sub>N<sub>4</sub>

- nanocomposite as heterojunction photocatalyst. *Diamond and Related Materials*, 133: 109716.
- 41. Karkeabadi, M., F. Nemati, A. Elhampour, and H.T. Nahzomi. (2019). Cu<sub>2</sub>O modified gC<sub>3</sub>N<sub>4</sub> as an effective catalyst for the synthesis of propargylamines: experimental, quantum mechanical mechanistic and kinetic study. *Reaction Kinetics, Mechanisms and Catalysis*, 126: 265-282.
- 42. Guo, S., N. Duan, Z. Dan, G. Chen, F. Shi, and W. Gao. (2018). g-C<sub>3</sub>N<sub>4</sub> modified magnetic Fe3O4 adsorbent: preparation, characterization, and performance of Zn(II), Pb(II) and Cd(II) removal from aqueous solution. *Journal of Molecular Liquids*, 258: 225-234.
- 43. Pang, H., Y. Jiang, W. Xiao, Y. Ding, C. Lu, Z. Liu, P. Zhang, H. Luo, and W. Qin. (2020). Facile synthesis of few-layer g-C<sub>3</sub>N<sub>4</sub> nanosheets anchored with cubic-phase CdS nanocrystals for high photocatalytic hydrogen generation activity. *Journal of Alloys and Compounds*, 839: 155684.
- 44. Ding, H., Q. Zhang, X. Yang, Q. Feng, D. Wang, and Z. Liu. (2023). A composite of biomass porous carbon supported g-C<sub>3</sub>N<sub>4</sub> by 2, 4, 6-triaminopyrimidine modification for enhancing oxytetracycline removal. *Journal of Applied Polymer Science*, 140(28): e54027.
- 45. Saravanan, V., P. Lakshmanan, and C. Ramalingan. (2023). Iron integrated carbon nitride: A recoverable heterogeneous catalyst for the construction of bis (hetero/homoarylidene) cycloalkanones. *Applied Organometallic Chemistry*, 37(10): e7215.
- 46. Taib, N.I., F.A. Latif, Z. Mohamed, and N.D.S. Zambri. (2018). Green synthesis of iron oxide nanoparticles (Fe<sub>3</sub>O<sub>4</sub>-NPs) using *Azadirachta indica* aqueous leaf extract. *International Journal of Engineering & Technology*, 7: 9-13.
- 47. Preeyanghaa, M., M. Dhileepan, J. Madhavan, and B. Neppolian. (2022). Revealing the charge transfer mechanism in magnetically recyclable ternary g-C<sub>3</sub>N4/BiOBr/Fe<sub>3</sub>O<sub>4</sub> nanocomposite for efficient photocatalytic degradation of tetracycline antibiotics. *Chemosphere*, 303: 135070.
- 48. Zambov, L.M., C. Popov, N. Abedinov, M.F. Plass, W. Kulisch, T. Gotszalk, P. Grabiec, I.W. Rangelow, and R. Kassing. (2000). Gas-sensitive properties of nitrogen-rich carbon nitride films. Advanced Materials, 12(9): 656-660.
- 49. Cao, S., J. Low, J. Yu, and M. Jaroniec. (2015). Polymeric photocatalysts based on graphitic carbon nitride. *Advanced Materials*, 27(13): 2150-2176.
- Dehbi, A., Y. Dehmani, D.S. Franco, H. Omari, J. Georgin, Y. Brahmi, K. Elazhari, M. Messaoudi, I. Aadnan, and T. Lamhasni. (2024). A statistical

- physics approach to understanding the adsorption of methylene blue onto cobalt oxide nanoparticles. *Molecules*, 29(2): 412.
- 51. Zhou, K., L. Yan, R. Zhang, and X. Zhu. (2023). Easily separated and sustainable cellulose-based adsorbent using a facile two-step modification for highly efficient methylene blue removal. *Biomass Conversion and Biorefinery*, 2023: 1-14.
- 52. Alghamdi, W.M. and I. El Mannoubi. (2021). Investigation of seeds and peels of Citrullus colocynthis as efficient natural adsorbent for methylene blue dye. *Processes*, 9(8): 1279.
- 53. Meena, P.L., J.K. Saini, A.K. Surela, B. Mordhiya, L.K. Chhachhia, and K.S. Meena. (2023). Fabrication of polyaniline-supported mno2 nanocomposite for removal of water pollutant: kinetic and isotherm studies. *ChemistrySelect*, 8(25): e202300724.
- 54. Bahrami, M., M.J. Amiri, S. Rajabi, and M. Mahmoudi. (2024). The removal of methylene blue from aqueous solutions by polyethylene microplastics: Modeling batch adsorption using random forest regression. *Alexandria Engineering Journal*, 95: 101-113.
- 55. Cai, X., J. Li, Y. Liu, X. Hu, X. Tan, S. Liu, H. Wang, Y. Gu, and L. Luo. (2020). Design and preparation of chitosan-crosslinked bismuth ferrite/biochar coupled magnetic material for methylene blue removal. *International Journal of Environmental Research and Public Health*, 17(1): 6.
- 56. Zouggari, H., F.-Z. Mahir, A. Imgharn, A. Hsini, N. Aarab, M. Laabd, and A. Albourine. (2023). Arginine-polyaniline@ g-C<sub>3</sub>N<sub>4</sub> for outstanding retention of Orange G dye from water. *Carbon Letters*, 33(6): 1897-1908.
- 57. Zghal, S., I. Jedidi, M. Cretin, S. Cerneaux, and M. Abdelmouleh. (2023). Adsorptive removal of Rhodamine B dye using carbon graphite/cnt composites as adsorbents: Kinetics, isotherms and thermodynamic study. *Materials*, 16(3): 1015.
- 58. Farhadi, H. and N. Keramati. (2023). Investigation of kinetics, isotherms, thermodynamics and photocatalytic regeneration of exfoliated graphitic carbon nitride/zeolite as dye adsorbent. *Scientific Reports*, 13(1): 14098.
- 59. Kuan, J., H. Zhang, H. Gu, Y. Zhang, H. Wu, and N. Mao. (2022). Adsorption-enhanced photocatalytic property of Ag-doped biochar/g-C<sub>3</sub>N<sub>4</sub>/TiO<sub>2</sub> composite by incorporating cottonbased biochar. *Nanotechnology*, 33(34): 345402.
- 60. Alharbi, R.A., F.M. Alminderej, N.F. Al-Harby, N.Y. Elmehbad, and N.A. Mohamed. (2023). Preparation and characterization of a new bisuracil chitosan-based hydrogel as efficient adsorbent for removal of anionic Congo red dye. *Polymers*, 15(6): 1529.

- 61. Antić, K., A. Onjia, D. Vasiljević-Radović, Z. Veličković, and S.L. Tomić. (2021). Removal of nickel ions from aqueous solutions by 2-hydroxyethyl acrylate/itaconic acid hydrogels optimized with response surface methodology. *Gels*, 7(4): 225.
- 62. Alwi, R.S., R. Gopinathan, A. Bhowal, and C. Garlapati. (2020). Adsorption characteristics of activated carbon for the reclamation of Eosin Y and indigo carmine colored effluents and new isotherm model. *Molecules*, 25(24): 6014.
- 63. Sulaiman, N.S., M.H. Mohamad Amini, M. Danish, O. Sulaiman, and R. Hashim. (2021). Kinetics, thermodynamics, and isotherms of methylene blue adsorption study onto cassava stem activated carbon. *Water*, 13(20): 2936.
- 64. Taguba, M.A.M., D.C. Ong, B.M.B. Ensano, C.-C. Kan, N. Grisdanurak, J.-J. Yee, and M.D.G. de Luna. (2021). Nonlinear isotherm and kinetic modeling of Cu (II) and Pb (II) uptake from water by MnFe<sub>2</sub>O<sub>4</sub>/chitosan nanoadsorbents. *Water*, 13(12): 1662.
- 65. Trazzi, P.A., M. Vashishtha, J. Najser, A. Schmalenberger, V.K. Kannuchamy, J.J. Leahy, and W. Kwapinski. (2024). Adsorption of ammonium, nitrate, and phosphate on hydrochars and biochars. *Applied Sciences*, 14(6): 2280.
- 66. Liu, C., N. Liu, X. Li, X. He, X. Liu, B. Hu, and S. He. (2022). Adsorption of Cd (II) on mesoporous Al<sub>2</sub>O<sub>3</sub> prepared from high-aluminum fly ash. *Materials Research Express*, 9(6): 065502.
- 67. Antonieti, C.C. and Y.P. Ginoris. (2022). Removal of cylindrospermopsin by adsorption on

- granular activated carbon, selection of carbons and estimated fixed-bed breakthrough. *Water*, 14(10): 1630.
- 68. Wonorahardjo, S., F. Fajaroh, R. Joharmawan, N. Nazriati, and E. Budiasih. (2023). Cadmium and lead ions adsorption on magnetite, silica, alumina, and cellulosic materials. *Scientific Reports*, 13(1): 4213.
- 69. Bhattacharya, S., N. Bar, B. Rajbansi, and S.K. Das. (2024). Adsorptive elimination of methylene blue dye from aqueous solution by chitosan-n SiO2 nanocomposite: Adsorption and desorption study, scale-up design, statistical, and genetic algorithm modeling. *Environmental Progress & Sustainable Energy*, 43(2): e14282.
- Azimi, E.B., A. Badiei, and J.B. Ghasemi. (2019). Efficient removal of malachite green from wastewater by using boron-doped mesoporous carbon nitride. *Applied Surface Science*, 469: 236-245.
- 71. Tian, L., J. Li, F. Liang, J. Wang, S. Li, H. Zhang, and S. Zhang. (2018). Molten salt synthesis of tetragonal carbon nitride hollow tubes and their application for removal of pollutants from wastewater. *Applied Catalysis B: Environmental*, 225: 307-313.
- 72. Ren, B., Y. Xu, L. Zhang, and Z. Liu. (2018). Carbon-doped graphitic carbon nitride as environment-benign adsorbent for methylene blue adsorption: Kinetics, isotherm and thermodynamics study. *Journal of the Taiwan Institute of Chemical Engineers*, 88: 114-120.